Article

Dopant-Free Spiro-OMe₂ Imidazole-Based Hole-Transporting Material for Stable and Low-Cost Organic−Inorganic Perovskite Solar Cell

Leila Haji-khan Mirzaei, Hashem Shahroosvand,* Afsaneh Farokhi, Elahe Bayat, Sebastiano Bellani,*
Cosimo Anichini, Mohsen Ameri, and Francesco Bonaccorso*

Read Online

ACCESS | Metrics & More | Article Recommendations | SI Supporting Information

ABSTRACT: The engineering of charge transport materials, with electronic characteristics that result in effective charge extraction and transport dynamics, is pivotal for the realization of efficient perovskite solar cells (PSCs). Herein, we elucidate the critical role of terminal substituent methoxy groups ($-OCH_3$) on the bandgap tuning of the spiro-like hole transport materials (HTMs) to realize performant and cost-effective PSCs. By considering spiro-OMeTAD as the benchmark HTM, we kept the backbone of spiro while replacing diphenylamine with phenanthrenimidazole. This approach significantly decreases the cost of spiro-OMeTAD by reducing the cost of the ancillary group from 0.051 to 0.012 \$/g. By increasing the number of methoxy groups on the ancillary ligand from four to eight, the power conversion efficiency (PCE) of the corresponding PSCs containing dopants passed from 17.10% to 18.70%, approaching the value achieved using spiro-OMeTAD containing dopants (PCE = 19.26%). Remarkably, the devices based on dopant-free spiro-OMeTAD have shown a significant loss of PCE, which

decreased from 12.9% to 10.1% after 300 h (to 8.2% after 600 h) of light soaking at an open circuit voltage. On the contrary, the cells based on the designed dopant-free HTM demonstrated optimal PCE retention, experiencing a minor drop from 14.4% to 14.1% and 13.2% after 300 and 600 h, respectively, of light soaking at open-circuit voltage.
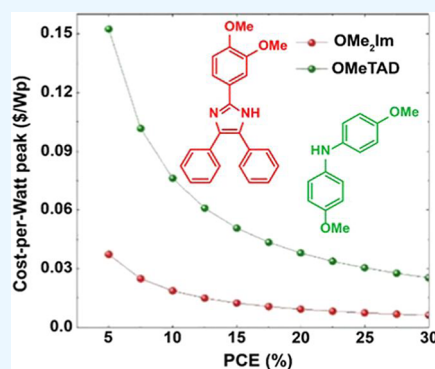
1. INTRODUCTION

Over the last few decades, organo-metal halide perovskite solar cells (PSCs) have shown a significant boost in performance, increasing their power conversion efficiencies (PCEs) from 3.8% to a certified value of 26.1%.[1] To propel this technology, forefront investigations strongly rationalize the importance of both compositional and interface engineering of PSCs.[2−5] By the anions and/or cations within the perovskite atomic structures, the direct bandgaps of perovskites have been modulated within the visible spectrum to guarantee light-harvesting from the visible to the near-infrared regions for both thin-film single-junction and tandem solar cells.[6−8] Beyond the high absorption coefficients of perovskites (e.g., $\sim 1.5 \times 10^4$ cm^{-1} at 550 nm for the prototypical $CH_3NH_3PbI_3$ perovskite[9]), their low nonradiative recombination rate and high carrier mobility[10,11] resulted in PCEs approaching the high-record ones achieved with inorganic solar cells.[12] In addition to the compositional engineering of the perovskite layer, the charge transport materials play a crucial role in the overall performance of the PSCs.[13−15] The electron and hole transport materials (ETMs and HTMS, respectively) can effectively facilitate the charge collection from the perovskite light absorber toward the current collectors while avoiding the occurrence of charge recombination processes.[14,16−18] Therefore, recent research projects have increasingly focused on the

engineering of both ETMs and HTMs to enhance the PCE and stability of the PCEs.[4,19−25] More in detail, effective charge transport materials must be designed with suitable energy levels,[26] while exhibiting satisfactory electrical conductivity and stability during PSC operational conditions. While viable ETLs (including TiO₂, SnO₂, and phenyl-C61-butyric acid methyl ester -PCBM-) have been widely established for efficient PSCs,[23] the most used HTMs still suffer from significant limitations, such as high cost,[27] long-term instability,[28] complex synthesis,[29] hygroscopicity, and incompatibility with nonhazardous solvents or even poor solubility.[30] As a striking example, 2,2′,7,7′-tetrakis[N,N-di(4-methoxyphenyl)amino]-9,9′-spirobifluorene (spiro-OMeTAD)[31] exhibits suitable energy levels for hole-extracting and electron blocking properties, yielding a PCE of corresponding PSCs as high as 25.17%.[2,32] However, the main drawbacks of spiro-OMeTAD are crystallization at the temperature of ∼85 °C (which can be
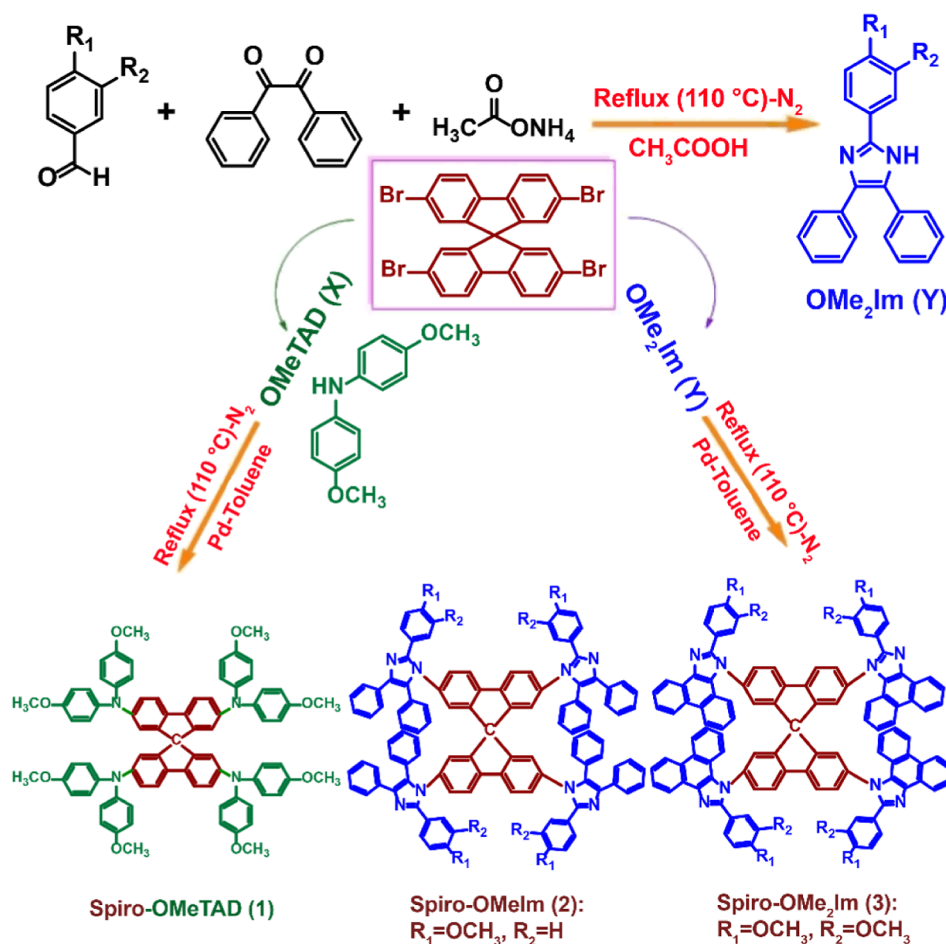
Figure 1. Synthetic procedures for spiro-OMeTAD (**1**), spiro-OMeIm (**2**), and spiro-OMe$_2$Im (**3**).

reached during device processing and even during their operation under 1 sun illumination),[33,34] low hole mobility in its pristine form,[35,36] as well as the high cost of production and purification,[28] along with the essential need for expensive catalysts (Pd)[27,37] for the synthetic process. To the best of our knowledge, the cost of spiro-OMeTAD with its six challenging production and purification steps, excluding the total cost of synthetic chemical wastes (3.6 g), can be estimated at approximately ~\$92 g^{-1}.[38] Furthermore, conventional p-dopants, such as Li-bis(trifluoromethanesulfonyl)-imide (Li-TFSI) and *tert*-butylpyridine (*t*BP) further deteriorate the long-term performance of PSCs[39,40] (by shifting the chemical equilibrium of the perovskite toward oxidized by-product),[41] while increasing either the complexity or the cost of the cell manufacturing. Recently, Wu et al. reported a green solvent processable dopant-free spiro-OMeTAD, which could be processed from nonhalogenated solvent tetrahydrofuran (THF), and the corresponding device has shown a high performance approaching 17%.[42] In the following, the same group reported a PCE of 16.94% for a control device based on a dopant-free spiro-OMeTAD device.[43] Therefore, it is important to identify new cost-effective HTMs that exhibit high hole mobility and operational stability.

In this context, many starburst and linear compounds have been designed as alternatives to conventional spiro-based HTMs.[44] However, it has been reported that PSCs with linear and starburst HTM compartments exhibit lower PCEs and stability in comparison to those based on spiro molecules.[44]

Therefore, there is an ongoing research effort on the synthesis of effective novel HTMs, fulfilling the desired balance between the cost of preparation, efficiency, and stability of the device.[45] In particular, the design of inexpensive dopant-free HTMs for PSCs with chemical stability superior to conventional HTMs provides an opportunity for the realization of cost-effective PSCs.[46] Several approaches have been proposed to overcome the unfavorable features of spiro-OMeTAD, either by modifying the position of the terminal substitutions in its structure[47] or by changing the conjugated atoms (side groups) attached to the spiro-based core.[48,49] For example, the electronic properties of spiro-based HTMs were tuned by displacing one of its methoxy groups (−OCH$_3$) from para to ortho positions, improving the PCE of the corresponding PSCs by ~11.3%.[47] In addition, imidazole moieties in organic molecules have been demonstrated to play a significant role in intramolecular and intermolecular interactions, such as hydrogen bonding, concerted proton−electron transfer (CPET), or excited-state intramolecular proton−electron of conjugation of phenanthroline-fused imidazole tetracyclic system (1*H*-phenanthro imidazole),[52] together with their facile incorporation into other molecules, making this organic structure a functional building block of spiro-based HTMs.[53] Besides, imidazole-based compounds have optimal thermal stability, tunable absorption wavelength from 300 to 550 nm, and a high molar extinction coefficient of over 10,000 M^{-1} cm^{-1}, which are key features for photovoltaic applications.[54,55] Only a few experimental studies have shown that the position of the
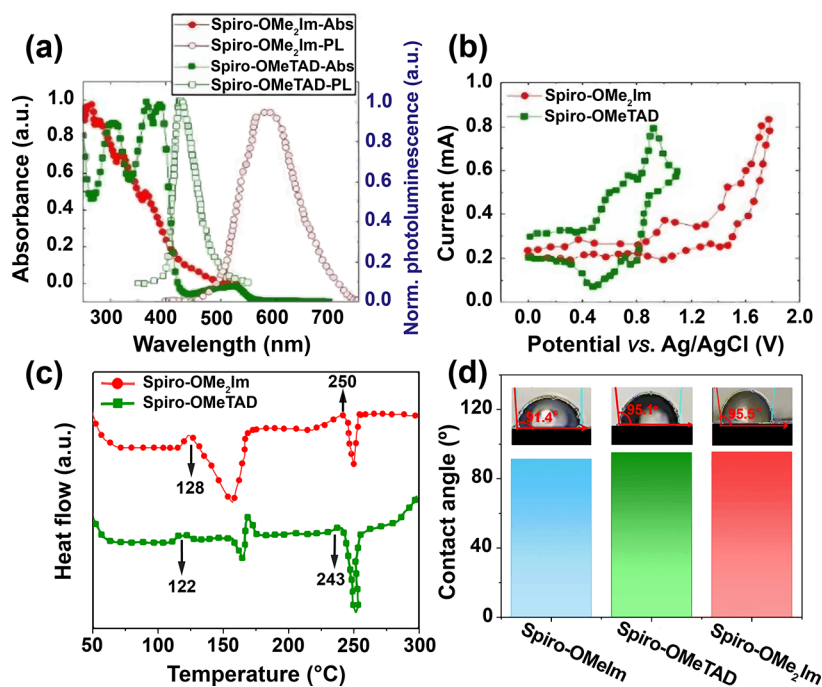
Figure 2. (a) UV−vis absorbance and PL spectra of (**3**) and (**1**) in CHCl₃. (b) CV curves of (**3**) and (**1**). (c) DSC curves of (**3**) and (**1**). (d) Water contact angles of (**3**), (**2**), and (**1**).

substitutions in an imidazole-based HTM is one of the variables mostly affecting the optical bandgap energies of the material. Based on these premises, the spiro-based compounds produced by attaching two methoxy phenyl groups to a 5-membered imidazole ring in the phenanthroimidazole framework as a terminal substituent of the spiro-based core[47] represent promising spiro-based HTMs to be directly compared with both spiro-OMeTAD and spiro-OMeIm with only one methoxy group (−OCH₃).[51] Therefore, in this work, we designed a new methodology for the synthesis of a low-cost imidazole-based derivative HTM (spiro-OMe₂Im) for PSCs. Our novel HTM enables the realization of PSCs with a PCE resembling those achieved using state-of-the-art HTMs, while significantly improving the device stability.

2. RESULTS AND DISCUSSION

Figure 1 shows the overall synthetic route of spiro-OMe₂Im (**3**), whose preparation procedures are thoroughly reported in the Experimental Section.

Briefly, this HTM was obtained via a two-step reaction, which includes (1) the synthesis of OMe₂Im precursor without relying on expensive catalysts or further purification steps (72% yield) and (2) Buchwald−Hartwig amination reaction between OMe₂Im and the widely available 2,2′,7,7′−tetrabromo−9,9′−spirobifluoren (59% yield), resulting in the final product. Compared to traditional spiro-OMeTAD (**1**) and our previously reported spiro-OMeIm (**2**), spiro-OMe₂Im (**3**) has a superior production yield and lower synthesis costs, making it a promising material to be investigated as a HTM (as shown hereafter). Consequently, several material characterizations, including ultraviolet−visible (UV−vis) absorbance spectroscopy, photoluminescence (PL), cyclic voltammetry (CV), and differential calorimetric scanning (DSC) measurements were carried out to elucidate the optoelectronic properties and thermal stability of (**3**).

The optoelectronic properties of the synthesized organic molecules were first characterized by UV−vis and PL measurements. As shown in Figure 2a, the absorbance spectrum of (**3**) exhibits four broad absorption bands in the 250−400 nm range. These bands correspond to intraligand charge-transfer (ILCT) processes. Compared to (**3**), (**1**) shows an absorbance spectrum over wavelengths extended up to ∼580 nm. To understand the influence of the terminal substitutions on the absorption onset wavelength and, consequently, on the optical bandgap, the absorbance spectrum of (**3**) was further compared to that of (**2**), as synthesized according to the synthesis reported in our previous work.[50] The data reveal that the first absorption peak of (**2**), located at 291 nm, is blue-shifted by 40 nm in (**3**), which implies an increase in the optical bandgap.[50] The PL spectrum of (**3**) shows a maximum emission at 583 nm, which is largely red-shifted by about 180 nm relative to the peak of the PL spectrum of (**1**). Moreover, the maximum emission band of (**2**) is located at 457 nm.[50] The large red shifts observed for (**3**) compared to both (**1**) and (**2**) can be attributed to the expansion of the conjugate system in (**3**). The energy of the lowest unoccupied molecular orbital (LUMO) can be calculated from the energy at which the intersection of the UV−vis and PL spectra occurs (E_{o-o}), according to the equation $E_{LUMO} = E_{HOMO} + E_{o-o}$, in which E_{HOMO} is the energy level of the highest occupied molecular orbital (HOMO).[52,56] Meanwhile, CV measurements can be used to determine the E_{HOMO} of each compound according to the equation, $E_{HOMO} = -(E_{ox}(\text{vs Ag/AgCl}) + 4.8 \text{ eV})$, in which E_{ox} is the potential of the first oxidation peak.[57] As shown by the cyclic voltammograms reported in Figure 2b, the E_{ox} of (**3**) occurs at 0.38 V vs Ag/AgCl, which is lower than the potential of the first anodic peak of (**1**) (0.6 V vs Ag/AgCl). These results indicate that (**3**) is more easily oxidized than (**1**). On comparing the cyclic voltammogram of (**2**) with that of (**3**), a similar shift of the E_{ox} of (**2**) with respect to (**1**) is observed (from 0.55 to 0.38 V vs

Ag/AgCl). The shift of E_{ox} is ascribed to the presence of only one electron donor group in the former (**2**), whereas (**3**) contains two donor groups. The subsequent oxidation peaks of (**3**) occur at potentials significantly higher than the first oxidation peak because of the high charge density in the phenanthroimidazole ring. The optoelectronic properties of the as-synthesized compounds, as extrapolated from UV−vis absorbance spectroscopy, PL, and CV measurements, are summarized in Table 1. These results indicate that the HOMO

Table 1. List of the Optoelectronic and Thermal Properties Measured for (1), (2), and (3)

HTM	(1)	(2)	(3)
λ_{max} abs[47a]	304, 378, 525	291,320(sh)	261, 281(sh), 319, 362
λ_{max} PL[47a]	425	457	583
HOMO[52b]	−5.2	−5.1	−5.0
LUMO[3c]	−2.2	−1.9	−2.4
T_m [°C][d]	248	>350	250
$\eta_{quenching}$[e]	0.91	0.87	0.76

[a]Data acquired from the analysis of the absorption spectra measured in 1×10^{-5} M chloroform ($CHCl_3$) solution. [b]Data calculated from CV measurements by using the following equation: $E_{HOMO} = -(E_{ox}(vs\ Ag/AgCl) + 4.8\ eV)$ in 0.1 M $CHCl_3$/tetrabutylammonium perchlorate (TBAP) vs Ag/AgCl at a scan rate of 100 mV/s. [c]Data is calculated by using the following equation: $E_{LUMO} = E_{HOMO} + E_{o-o}$. [d]Data obtained from DSC. [e]$\eta_{quenching} = (PL_{bare} - PL_{quench})/PL_{bare}$, in which PL_{bare} and PL_{quench} are the cumulative PL intensities of perovskite on sapphire substrates with and without the HTM substrate, respectively. Sh = Shoulder.

of (**3**) (∼−5.0 eV) is similar to that of (**1**) (∼−5.2 eV) and (**2**) (∼−5.1 eV) and well-aligned with the valence band of the methylammonium (MA)-/formamidinium (FA)-based perovskite used in this work (∼−5.4 eV).

Differential scanning calorimetry measurements were performed to evaluate the thermal stability of both (**3**) and (**1**). As shown in Figure 2c, the glass transition temperature (T_g) of (**3**) and (**1**) are 128 and 122 °C, respectively, which are higher than the temperatures at which perovskites typically degrade (≥90 °C).[58] Furthermore, the melting point of (**3**) is 250 °C, which is very close to that of (**1**) (248 °C).[59] Thus, these findings suggest that (**3**) displays a thermal stability similar to that of (**1**). Another important property required by the HTM to improve the PSC stability relates to the ability to contrast the water and moisture access toward the perovskite layer. Therefore, water contact angle measurements were performed on the surface of HTMs to evaluate their hydrophobicity. As shown in Figure 2d, (**3**) displays a water contact angle of 95.5°, indicating a hydrophobicity higher than those of (**1**) and (**2**) (water contact angles of 95.1° and 91.4°, respectively).

Based on their characterizations, the as-synthesized products were used as HTMs in PSCs. The latter were fabricated according to the mesoscopic configuration: fluorine tin oxide (FTO)-coated glass/compact TiO_2 (bl-TiO_2)/mesoporous TiO_2 (meso-TiO_2)/$(FAPbI_3)_{0.85}(MAPbBr_3)_{0.15}$/spiro-OMe_2Im or spiro-OMeTAD or spiro-OMeIm containing dopants/Au, as sketched in Figure 3a. Figure 3b shows the SEM image of a representative PSC with (**3**) as the HTM containing dopants, evidencing its layered configuration. According to previous studies and preliminary characterizations, the thickness of the hole transport layer was set to ∼200 nm.[60] Importantly, no defects or pores are observed in
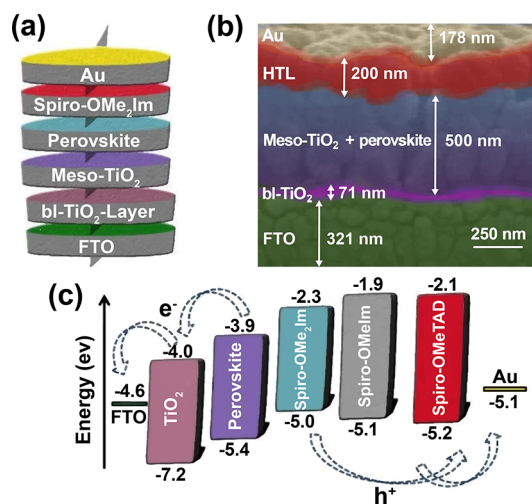

Figure 3. (a) Schematic sketch of the investigated PSC configurations using (**3**) as the HTM. (b) Cross-sectional SEM image of representative PSCs based on (**3**) containing dopants, and (c) energy diagram of the materials composing the PSC.

the PSC layers, indicating a homogeneous pinhole-free deposition of the latter. The structural characteristics of the perovskite/HTM interface, as well as the energy level (mis)match between the perovskite and HTM, have a crucial role in the photovoltaic performance of the PSCs. In particular, an ideal HTM must simultaneously display optimal hole transport properties and HOMO level matching with the maximum energy of the valence band of the perovskite.[61] As a rule of thumb, a small driving energy (∼0.07 eV) is required to induce highly efficient hole transfer from the perovskite to the HTM.[62] This means that an interfacial energy offset in the range of 0.07−0.18 eV is pursued to maximize the open-circuit voltage (V_{OC}) of the cell while achieving high short-circuit current density (J_{SC}) and high fill factor (FF). Compared to (**2**), whose HOMO and LUMO energy levels are ∼ −5.1 and ∼ −1.9 eV, respectively, (**3**) exhibits higher HOMO and lower LUMO energy levels due to the presence of a second methoxy group in its framework.[61] This phenomenon stems mainly from the distribution of the HOMO and LUMO orbitals in the terminal substituents. Moreover, some previous studies supported that the methoxy groups in the HTM structure modify the HOMO level of the material.[63] Even more, methoxy groups play a significant role in adhering the HTM to the underlying perovskite layer.[63] Noteworthy, the electron-donating or -withdrawing nature of methoxy substituents depends on their particular position and interaction with the attached ring,[64] which has to be controlled for the specific design of HTMs. Based on the above considerations, as well as the HOMO level measured for our HTMs, the oxygen in the methoxy group of (**3**) likely acts as a donor, and its resonance effect can prevail on its induction effect.[65] In other words, the introduction of two donor groups can stabilize the LUMO level and destabilizes the HOMO one in our new HTM (**3**). Consequently, we predicted that (**3**) is able to lose its electrons more easily[66,67] than (**2**), providing hole-collecting and transporting abilities.[64,65]

Steady-state PL spectroscopy measurements were performed to assess the ability of the HTMs to extract the photogenerated holes from the perovskite layer. In fact, the hole extraction process hinders the radiative charge recombination in the

absorber material,[68] whose PL is therefore quenched. As shown in Figure 4a, both (1) and (3) efficiently quenched the
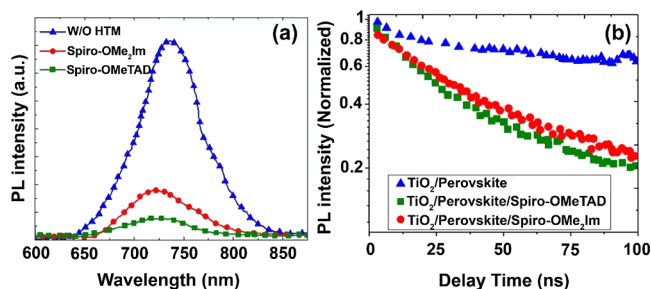

Figure 4. (a) Steady-state PL spectra measured for perovskite layer with and without HTLs ((1) and (3)). (b) TRPL curves measured for TiO_2/perovskite, TiO_2/perovskite/spiro-OMe$_2$Im (doped), and TiO_2/perovskite/spiro-OMeTAD (doped).

PL of the perovskite. The PL quenching efficiency (η_{quench}) can be calculated by the equation: $\eta_{quench} = (PL_{bare} - PL_{quench})/PL_{bare}$, in which PL_{bare} and PL_{quench} are the cumulative PL intensities of perovskite on sapphire substrates with and without the HTM layer, respectively.[69] As also reported in Table 1, a high η_{quench} (>0.70) has been measured for all three spiro-based compounds, which can therefore inhibit radiative charge recombination processes, thus acting as efficient HTMs.[64]

Time-resolved photoluminescence spectroscopy (TRPL) measurements were carried out to evaluate the charge carrier extraction dynamics in the doped spiro-OMe$_2$Im-based device in comparison with those in spiro-OMeTAD-based and hole-transporting layer (HTL)-free cells. As shown in Figure 4b, the TRPL curves show a nonexponential decay. By fitting the TRPL curves with a biexponential decay function, the estimated photocharge lifetimes for TiO_2/perovskite, TiO_2/perovskite/spiro-OMe$_2$Im (doped), and TiO_2/perovskite/spiro-OMeTAD (doped) were 80.20, 55.42, and 48.16 ns, respectively. Thus, TRPL data are consistent with the steady-state PL results and indicate that the new spiro-OMe$_2$Im has a promising charge extraction ability similar to that of spiro-OMeTAD.

Figure 5a shows the photocurrent density−voltage (J−V) curves measured for the PSCs based on HTM (3) containing dopants under AM 1.5G (100 mW/cm²) illuminations in both backward (BW) and forward (FW) voltage scan modes. These curves are compared with those recorded for the PSCs based on (1) as the HTM containing dopants. As summarized in

Table 2, the data demonstrate that the device used on (3) containing dopants exhibits a PCE as high as 18.7%, which is

Table 2. List of the Photovoltaic Parameters Measured for the PSCs Using Different HTLs-Containing Dopants

HTM	V_{OC} [V]	J_{SC} [mA cm^{-2}]	FF [%]	PCE [%]
spiro-OMe$_2$Im-FW	1.120	22.63	69	18.70
spiro-OMe$_2$Im-BW	1.123	22.36	73	18.70
spiro-OMeTAD-FW	1.13	22.17	78	19.26
spiro-OMeTAD-BW	1.12	21.95	77	18.81
spiro-OMeIm-FW	1.10	20.46	76	17.10
spiro-OMeIm-BW	1.10	20.35	75	16.78
w/o HTM	0.66	7.86	49	2.25

nearly comparable to the PCE measured for the (1)-based PSCs containing dopants (PCE = 19.26%). In addition, both of the PSC configurations show negligible hysteresis. Noteworthy, similar PSCs using the same device architecture with (2) as the HTM-containing dopants reached a PCE of 17.10%, which was ∼1.6% lower than the PCE measured for devices using HTM (3). This PCE difference between the cells indicates that the two ($-OCH_3$) groups in the newly designed HTM provide better hole-extraction properties compared to only one ($-OCH_3$) terminal donor group in (2).

The difference between the HOMO level of the HTM and the quasi-Fermi levels of TiO_2 approximately determines the V_{OC} of PSCs.[67] As shown from the values reported in Table 2, the increase of the number of methoxy groups increases the V_{OC} of our cells, which shows a maximum V_{OC} of 1.123 V when (3) is used as HTM. This effect can be explained by the higher driving energy regulating the hole transfer from the perovskite to the HTM (3) compared to (2), in agreement with the HOMO levels reported in Table 1.[70] As a consequence of the same effect, the PSC based on (2) also shows a lower J_{SC} (20.46 mA cm^{-2}) compared to the one measured for the device based on (3).[70] In contrast, PSCs based on (3) and (1) show both similar V_{OC} (1.20 and 1.13 V, respectively) and J_{OC} (22.63 and 22.17 mA cm^{-2}, respectively), indicating that the proposed HTM (3) is an optimal candidate to replace (1) in state-of-the-art devices. Figure 5b shows the external quantum efficiency (EQE) spectrum measured for PSCs with our new HTM (3) containing dopants, compared to the one recorded for cell-based (1) containing dopants. The integrated current density ($J_{SC,calc}$, calculated from the EQE data in the 300−800 nm range under AM1.5G conditions) for the devices is consistent with the J−V curve data (i.e., $J_{SC,calc}$.
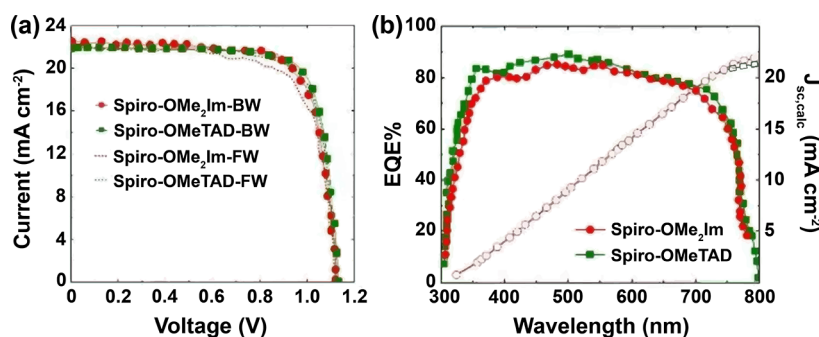

Figure 5. (a) J−V curve measured for the PSCs using (3) and (1) HTMs-containing dopants in forward (FW) and backward (BW) voltage scan modes and (b) corresponding EQE spectra together with calculated integrated short-circuit photocurrent density ($J_{SC,calc}$) curves.

$\sim J_{SC}$). In particular, the PSCs based on compound (**3**) show a maximum EQE of 84.3% at 495 nm.

Figure 6 reports the statistical analysis of the photovoltaic parameters recorded for the PSCs based on different HTLs-containing dopants.
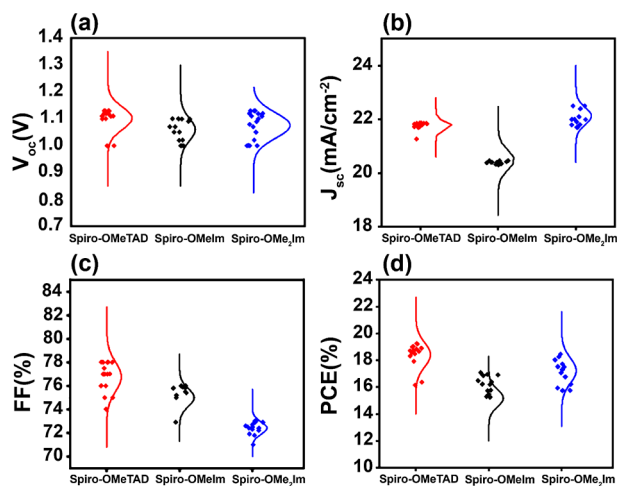

Figure 6. Statistical analysis of (a) V_{OC}, (b) J_{SC}, (c) FF, and (d) PCE measured for the PSCs based on spiro-OMeTAD (**1**)-, spiro-OMeIm (**2**)-, and spiro-OMe$_2$Im (**3**)-containing dopants.

The long-term stability of the PSC is also another requirement for the commercial exploitation of this perovskite-based photovoltaic technology. Therefore, the stability of PSCs based on HTMs (**3**) and (**1**) for the two types, dopant-free and containing dopants, was evaluated over 600 h (the details on the dopants are reported in Experimental Section). Stability tests were carried out on nonencapsulated devices at an ambient temperature with a controlled humidity of 30%. As shown in Figure 7, the device based on (**3**) with dopants exhibits a PCE that is significantly more stable than the PCE of the reference device based on (**1**) with dopants. In particular,
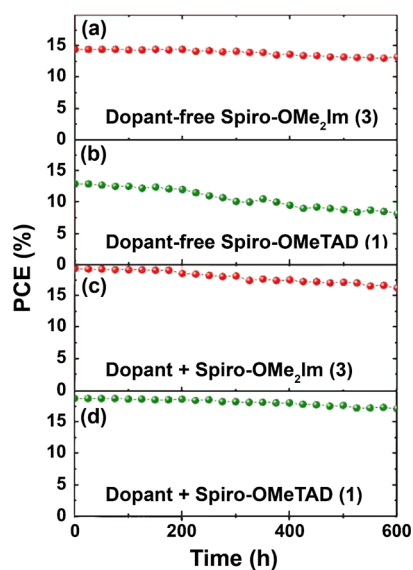

Figure 7. Stability of the PCE of the PSCs based on (a) dopant-free spiro-OMe$_2$Im (**3**) and (b) spiro-OMeTAD (**1**) and (c) doped (**3**) and (d) (**1**).

the PCE of the (**3**)-based device slightly decreased from 18.7% to 17.1% over 600 h, while the PCE of the (**1**)-based cell decreased from 19.26% to 16.2%. In addition, the cell using dopant-free (**1**) as the HTM experienced a nearly exponential decay from 12.9% to 10.1% over 300 h and to 8.2% after 600 h. In contrast, the dopant-free (**3**)-based cell was more stable and capable of retaining its initial PCE, which only decreased from 14.4% to 14.1% and 13.2% after 300 and 600 h, respectively. By considering both the PCE and the stability data, our dopant-free HTM (**3**) represents a potential cost-effective candidate for the implementation of both stable and efficient PSCs.

Atomic force microscopy (AFM) measurements were carried out on different HTLs to evaluate their thin-film-forming properties. Figure 8a,b shows the topographic AFM
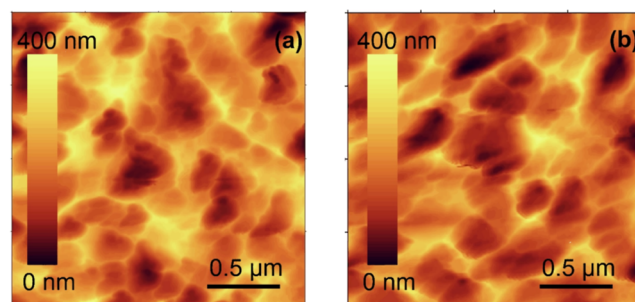

Figure 8. AFM images of (a) spiro-OMe$_2$Im film and (b) spiro-OMeTAD film.

images of spiro-OMe$_2$Im and spiro-OMeTAD, respectively, when deposited on glass substrates. These images indicate that the HTLs exhibit pinhole-free morphologies. The spiro-OMe$_2$Im film shows grain sizes larger than those of spiro-OMeTAD, suggesting high diffusion lengths of the charge carriers and reduced charge recombination associated with grain boundaries. Such morphology can result in the higher J_{SC} observed for spiro-OMe$_2$Im-based devices compared to that of spiro-OMeTAD-based reference cells.

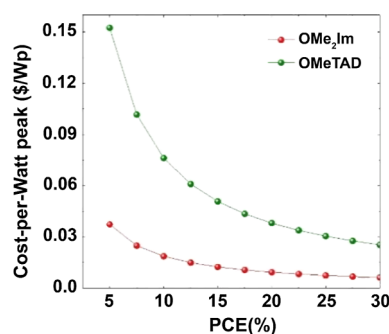Figure 9 shows the cost per watt peak (C_w) of the HTM precursors (OMe$_2$Im and OMeTAD), as calculated from the

Figure 9. Cost per watt peak ($ W p^{-1}) of (**1**) and (**3**) as a function of the PCE.

equation,[51] $C_w = \frac{(C_g \times P \times t)}{\eta \times I}$, in which C_g, P, η, and I represent the cost per gram of material, the density of the material, the efficiency of the corresponding PSC (from 5 to 30%), and the thickness of the HTM, respectively. These data clearly indicate that the synthesized OMe$_2$Im precursor is not only significantly

cheaper than OMeTAD but also comparable with OMeIm reported in our previous research. For example, for 15% PCE, the estimated cost for OMe$_2$Im is ∼ \$0.012 W p^{-1}, which is 75.4% lower than the price of conventional OMeTAD.

Figure 10 shows the comparison between the PCEs and the cost of the preparation for different HTMs, indicating the
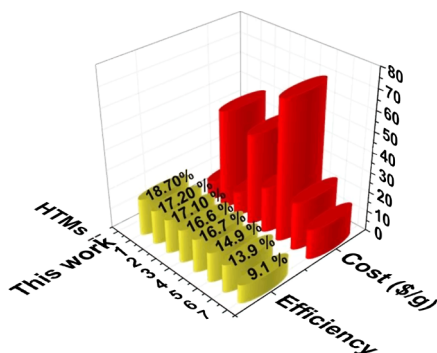

Figure 10. Pre-preparation cost of our HTM (**3**) and the PCE of the corresponding device in comparison with those obtained for other similar HTMs reported in literature.

advantages of our novel HTM over similar materials in terms of both the PCE and costs. For example, the PCE of HTM (**3**) (18.70%) is higher than those of other HTMs, while the preparation cost is as low as \$12 g^{-1}. The detailed photovoltaic and structural information on all HTMs shown in Figure 10 are presented in Table S1.

3. CONCLUSIONS

A new spiro compound based on imidazole groups functionalized with eight methoxy moieties has been designed, synthesized, and validated as a performant and cost-effective HTM in PSCs. The synthesis methodology of the new HTM was based on the one already used for spiro-OMeTAD. In more detail, we retained the spiro-backbone, while the diphenylamine was replaced with phenanthrenimidazole. The material structure allows reducing the total cost of spiro-OMeTAD via replacing the diphenylamine ancillary ligand, whose synthesis is catalyzed by expensive palladium catalysts. This study highlights the importance of terminal methoxy groups (−OCH$_3$) in tuning the bandgap of spiro-like HTMs for efficient and cost-effective PSCs. Increasing the number of methoxy groups from four to eight on the ancillary ligand led to a significant improvement in PCE from 17.10% to 18.70%, nearing the performance of spiro-OMeTAD (PCE = 19.26%). On comparing two materials, namely, spiro-OMeIm (**2**) and spiro-OMe$_2$Im (**3**), it was observed that (**3**) with an additional methoxy group exhibited higher HOMO and lower LUMO energy levels compared to (**2**). The presence of a second methoxy group in (**3**) acted as a donor, stabilizing the LUMO level and destabilizing the HOMO level. This suggests that (**3**) can easily lose electrons, enhancing its hole-collecting and transporting capabilities. Thus, the presence of the methoxy groups in (**3**) resulted in a V_{OC} as high as 1.123 V. The introduction of the imidazole functionality into the HTMs reduces the first oxidation potential compared to that of the benchmark spiro-OMeTAD (**1**), approaching the HOMO energy level of the perovskite. Furthermore, lowering the oxidation potential also results in a HOMO energy level that matches well with the valence band of the perovskite. We

attribute this phenomenon to the extended π-system of the imidazole substituents over their diphenyl counterparts in spiro-OMeTAD. Moreover, free-dopant PSCs based on our new HTM show a stable behavior over 600 h, while devices based on free-dopant spiro-OMeTAD rapidly degrade. In summary, this research presents a promising route for the discovery of new efficient and cost-effective HTMs based on a spiro-backbone, highlighting the challenges in the synthesis technique that still need to be addressed, optimizing photovoltaic efficiency, and reducing the overall cost of PSC technology.

4. EXPERIMENTAL SECTION

4.1. Materials. Solvents used for the synthesis were reagent grade and were used without any further purification. HPLC-grade solvents were used for the spectroscopic studies. All chemical substances were purchased from Sigma-Aldrich and Merck with a purity of 99% and were used without further purification.

4.1.1. Synthetic Procedures. 4.1.1.1. 2-(4,3-Methoxyphenyl)1H-phenanthro[9,10−d]imidazole (OMe$_2$Im). First, 0.136 g (1 mmol) of 3,4-dimethoxy benzaldehyde was added to 10 mL of acetic acid in a 100 mL two-necked flask, and the resulting mixture was mixed under a N$_2$ atmosphere for 10 min. After dissolving benzil in the solution, 3.854 g (50 mmol) of ammonium acetate was added to the solution, and the resulting mixture was heated to 127 °C. The mixture was then refluxed in an oil bath for 15 h. The resulting mixture was diluted with distilled water. Afterward, 1.5 to 2 mL of ammonia was introduced to the mixture to neutralize its pH. The product was dehydrated via a solvent extraction method using chloroform solvent and magnesium sulfate (MgSO$_4$). After evaporation of the chloroform solvent, the resulting cream-colored precipitate was collected with a yield of 72%. ^{1}H NMR (DMSO, 500 MHz): δ = 9.097(S, 1H), 8.574 (d, 2H), 8.409 (d, 2H), 7.759 (q, 2H), 7.315 (q, 2H), 7.261 (d, 1H), 7.219 (s, 1H), 6.085 (d, 1H), and 3.575 (s, 6H). CHN: Anal. Calcd for C$_{23}$H$_{20}$N$_2$O$_2$ (%): C, 77.512; H, 5.665; N, 7.864. Found (%): C, 77.516; H, 5.66; N, 7.861. ESI-MS: *m/z* 355.11, [M − H]$^+$.

4.1.1.2. Spiro-OMe$_2$Im. 0.158 g (0.25 mmol) of 2,2′,7,7′-tetrabromo-9,9′-spirobi[9Hfluorene], 0.35 g (1 mmol) of 2-(4,3-methoxyphenyl)1H-phenanthro[9,10−d]imidazole (OMe$_2$Im), and 1.922 g (5.8 mmol) of tris(dibenzilidene-actone)dipalladium (0): BINAP: sodiumtertbutoxide (0.05:0.15:2) were added in a 50 mL two-necked container. Subsequently, anhydrous toluene (10 mL) was poured into the flask under a N$_2$ atmosphere. The solution was heated under a N$_2$ atmosphere to 110 °C for 12 h. After cooling to room temperature, the resulting solution was extracted with an ethyl acetate and brine mixture (1:2). Then, the solvent was dried with anhydrous MgSO$_4$. The residue was filtered using silica-gel by column chromatography and eluted with a 1:8 solvent of ethyl acetate and hexane, obtaining spiro-OMe$_2$Im as an orange solid in a yield of 59%. ^{1}H NMR (CDCl$_3$, 500 MHz): δ = 8.711 (d, 8H), 8.689 (d, 8H),8.545 (q, 8H), 7.789 (q, 8H), 7.652 (d, 4H), 7.538 (d, 4H), 7.116 (s, 4H), 6.996 (s, 4H), 6.826 (d, 4H), 6.662 (d, 4H), and 3.73 (d, 24H). ^{13}C NMR (CDCl$_3$, 125 MHz): δ = 150.01, 149.19, 139.56, 131.75, 128.33, 127.31, 127.09, 125.23, 123.66, 123.03, 121.90, 121.70, 118.99, 111.0, 109.47, 77.54, 77.03, 76.52, 55.77, 55.54, 37.09, 32.75, 31.93, 29.71, 27.09, 24.46, 22.70, 19.47, 14.15, and 11.44. CHN: Anal. Calcd for C$_{117}$H$_{88}$N$_8$O$_8$, (%): C, 81.042; H,

5.126; N, 6.46. Found (%): C, 81.048; H, 5.121; N, 6.462; ESI-MS: m/z 1732.61, $[M - H]^+$.

4.1.2. Compound Characterization. ^{1}H NMR measurements were carried out by using a Bruker 250 MHz spectrometer in CDCl$_3$. UV−vis and PL spectra were measured by using an Ultrospec 3100 pro UV/visible spectrophotometer (in CHCl$_3$ solution) and Varian-Cary Eclipse fluorescence spectrophotometer, respectively. Electrochemical measurements were performed using a SAMA500 potentiostat electrochemical analyzer in a three-electrode configuration, using a Pt disk as the working electrode and a Pt wire as the counter electrode. The reference electrode was a Ag/AgCl reference electrode with saturated KCl, and 0.1 M TBAP in CHCl$_3$ was used as the supporting electrolyte.

4.1.3. PSC Fabrication. A piece of FTO-coated glass was etched with Zn powder and 2 M HCl in ethanol solvent, followed by washing with detergent, distilled water, acetone, and ethanol for cleaning the substrate. The glass was treated for 15 min using an ultraviolet/O$_3$ cleaner. Then, a film of bl-TiO$_2$ was coated on the FTO surface by spin-coating (2000 rpm) for 30 s with a titanium isopropoxide (TTIP) acidic solution. Afterward, the surfaces were heated to 500 °C for 30 min and cooled down to room temperature. To create a 300−400 nm thick mesoporous TiO$_2$ layer, diluted TiO$_2$ in ethanol precursor was spin-coated onto the bl-TiO$_2$/FTO substrate at 2000 rpm for 10 s, followed by calcination at 500 °C for 30 min to remove the organic part. Subsequently, a PbI$_2$ solution was spin-coated onto mesoporous TiO$_2$ at 6500 rpm for 5 s. Next, a mixed perovskite precursor solution was prepared by dissolving PbI$_2$ (1.15 M), formamidinium iodide (FAI) (1.10 M), PbBr$_2$ (0.2 M), and methylammonium bromide (MABr) (0.2 M) in anhydrous solvent N,N-dimethylformamide (DMF):dimethyl sulfoxide (DMSO) (4:1 vol/vol). The so-prepared solution was spin-coated using a two-step procedure at 1000 and 5000 rpm for 90 and 30 s, respectively. Spiro-OMeTAD (**1**), spiro-OMeIm (**2**), and spiro-OMe$_2$Im (**3**) were prepared at a concentration of 78 mM in chlorobenzene. Moreover, 18 μL of LiTFSI (from a stock solution in acetonitrile with a concentration of 1.0 M) and 29 μL of *tert*-butylpyridine (from a stock solution in chlorobenzene with a concentration of 1.0 M) were introduced as additives in the (**1**), (**2**), and (**3**) solutions. The HTM solution was deposited onto the perovskite layer by spin-coating at 4000 rpm for 20 s, forming the HTL. Finally, the Au electrode was deposited by thermal evaporation under a high vacuum (10^{-5} Pa).

4.1.4. Device Characterization. Current density−voltage ($J−V$) curves were recorded with a solar simulator (Newport, oriel Class A, 91195A) with a source meter (Keithley 2420) under the illumination of 100 mW/cm^2 (AM 1.5 G) and a calibrated Si-reference cell validated by National Renewable Energy Laboratory (NREL). The $J−C$ curves of the devices were acquired over an active area of 0.096 cm^2 defined by a metallic mask, using a voltage scan rate of 0.01 V s^{-1}. The light-soaking stability test was measured at continuous illumination with a 420 nm long-pass UV-filter under AM 1.5G at room temperature and in a N$_2$-filled glovebox. Moisture stability was measured for unencapsulated devices stored in relative humidity ranging between 30% and 60% at room temperature in the dark.

■ ASSOCIATED CONTENT

Ⓢ Supporting Information

The Supporting Information is available free of charge at https://pubs.acs.org/doi/10.1021/acsomega.4c05440.

PCE performances of PSC based on different spiro-cyclic HTL in relevant literature and synthesis cost of spiro-OMe$_2$Im (PDF)

■ AUTHOR INFORMATION

Corresponding Authors

Hashem Shahroosvand − *Group for Molecular Engineering of Advanced Functional Materials (GMA), Chemistry Department, University of Zanjan, 45617 Zanjan, Iran;* ⓞ orcid.org/0000-0001-9185-5490; Email: shahroos@znu.ac.ir

Sebastiano Bellani − *BeDimensional S.p.A., 16163 Genova, Italy;* ⓞ orcid.org/0000-0002-3576-1702; Email: s.bellani@bedimensional.it

Francesco Bonaccorso − *BeDimensional S.p.A., 16163 Genova, Italy; Graphene Laboratories, Istituto Italiano di Tecnologia, 16163 Genova, Italy;* Email: f.bonaccorso@bedimensional.it

Authors

Leila Haji-khan Mirzaei − *Group for Molecular Engineering of Advanced Functional Materials (GMA), Chemistry Department, University of Zanjan, 45617 Zanjan, Iran*

Afsaneh Farokhi − *Group for Molecular Engineering of Advanced Functional Materials (GMA), Chemistry Department, University of Zanjan, 45617 Zanjan, Iran*

Elahe Bayat − *Group for Molecular Engineering of Advanced Functional Materials (GMA), Chemistry Department, University of Zanjan, 45617 Zanjan, Iran*

Cosimo Anichini − *BeDimensional S.p.A., 16163 Genova, Italy*

Mohsen Ameri − *Department of Electrical and Computer Engineering, The University of Alabama, Tuscaloosa, Alabama 35487, United States;* ⓞ orcid.org/0000-0003-0453-5021

Complete contact information is available at:
https://pubs.acs.org/10.1021/acsomega.4c05440

Notes

The authors declare no competing financial interest.

■ REFERENCES

(1) (a) NREL. *Solar Cell Efficiency Chart Cell Efficiency Chart Photovoltaic Research*; NREL, 2021. (b) Yoo, J. J.; Seo, G.; Chua, M. R.; Park, T. G.; Lu, Y.; Rotermund, F.; Kim, Y.-K.; Moon, C. S.; Jeon, N. J.; Correa-Baena, J.-P.; Bulovic,́ V.; Shin, S. S.; Bawendi, M. G.;

Seo, J. Efficient Perovskite Solar Cells via Improved Carrier Management. *Nature* **2021**, *590*, 587−593. (c) Jeong, J.; Kim, M.; Seo, J.; Lu, H.; Ahlawat, P.; Mishra, A.; Yang, Y.; Hope, M. A.; Eickemeyer, F. T.; Kim, M.; Yoon, Y. J.; Choi, I. W.; Darwich, B. P.; Choi, S. J.; Jo, Y.; Lee, J. H.; Walker, B.; Zakeeruddin, S. M.; Emsley, L.; Rothlisberger, U.; Hagfeldt, A.; Kim, D. S.; Grätzel, M.; Kim, J. Y. Pseudo-Halide Anion Engineering for α-FAPbI₃ Perovskite Solar Cells. *Nature* **2021**, *592*, 381−385.

(2) Pashaei, B.; Bellani, S.; Shahroosvand, H.; Bonaccorso, F. Molecularly Engineered Hole-Transport Material for Low-Cost Perovskite Solar Cells. *Chem. Sci.* **2020**, *11*, 2429−2439.

(3) Llanos, M.; Yekani, R.; Demopoulos, G.; Basu, N. Alternatives Assessment of Perovskite Solar Cell Materials and Their Methods of Fabrication. *Renewable Sustainable Energy Rev.* **2020**, *133*, 110207.

(4) Ameri, M.; Ghaffarkani, M.; Ghahrizjani, R. T.; Safari, N.; Mohajerani, E. Phenomenological Morphology Design of Hybrid Organic-Inorganic Perovskite Solar Cell for High Efficiency and Less Hysteresis. *Sol. Energy Mater. Sol. Cells* **2020**, *205*, 110251.

(5) Lu, H.; Krishna, A.; Zakeeruddin, S. M.; Grätzel, M.; Hagfeldt, A. Compositional and Interface Engineering of Organic-Inorganic Lead Halide Perovskite Solar Cells. *Iscience* **2020**, *23*, 101359.

(6) Manser, J. S.; Christians, J. A.; Kamat, P. V. Intriguing Optoelectronic Properties of Metal Halide Perovskites. *Chem. Rev.* **2016**, *116*, 12956−13008.

(7) Lamanna, E.; Matteocci, F.; Calabrò, E.; Serenelli, L.; Salza, E.; Martini, L.; Menchini, F.; Izzi, M.; Agresti, A.; Pescetelli, S.; Bellani, S.; Del Rio Castillo, A. E.; Bonaccorso, F.; Tucci, M.; Di Carlo, A. Mechanically Stacked, Two-Terminal Graphene-Based Perovskite/Silicon Tandem Solar Cell with Efficiency over 26%. *Joule* **2020**, *4*, 865−881.

(8) Romano, V.; Najafi, L.; Sutanto, A. A.; Schileo, G.; Queloz, V.; Bellani, S.; Prato, M.; Marras, S.; Nazeeruddin, M.; D'Angelo, G.; Bonaccorso, F.; Grancini, G. Two-Step Thermal Annealing: An Effective Route for 15% Efficient Quasi-2D Perovskite Solar Cells. *ChemPlusChem* **2021**, *86*, 1044−1048.

(9) Park, N.-G. Perovskite Solar Cells: An Emerging Photovoltaic Technology. *Mater. Today* **2015**, *18*, 65−72.

(10) Xing, G.; Mathews, N.; Sun, S.; Lim, S. S.; Lam, Y. M.; Grätzel, M.; Mhaisalkar, S.; Sum, T. C. Long-Range Balanced Electron- and Hole-Transport Lengths in Organic-Inorganic CH₃NH₃PbI₃. *Science* **2013**, *342*, 344−347.

(11) Stranks, S. D.; Eperon, G. E.; Grancini, G.; Menelaou, C.; Alcocer, M. J.; Leijtens, T.; Herz, L. M.; Petrozza, A.; Snaith, H. J. Electron-Hole Diffusion Lengths Exceeding 1 Micrometer in an Organometal Trihalide Perovskite Absorber. *Science* **2013**, *342*, 341−344.

(12) Krishnamoorthy, T.; Kunwu, F.; Boix, P. P.; Li, H.; Koh, T. M.; Leong, W. L.; Powar, S.; Grimsdale, A.; Grätzel, M.; Mathews, N.; et al. A Swivel-Cruciform Thiophene Based Hole-Transporting Material for Efficient Perovskite Solar Cells. *J. Mater. Chem. A* **2014**, *2*, 6305−6309.

(13) Lim, K.; Kang, M.-S.; Myung, Y.; Seo, J.-H.; Banerjee, P.; Marks, T. J.; Ko, J. Star-Shaped Hole Transport Materials with Indeno [1, 2-b] thiophene or Fluorene on A Triazine Core for Efficient Perovskite Solar Cells. *J. Mater. Chem. A* **2016**, *4*, 1186.

(14) Ravishankar, S.; Gharibzadeh, S.; Roldán-Carmona, C.; Grancini, G.; Lee, Y.; Ralaiarisoa, M.; Asiri, A. M.; Koch, N.; Bisquert, J.; Nazeeruddin, M. K. Influence of Charge Transport Layers on Open-Circuit Voltage and Hysteresis in Perovskite Solar Cells. *Joule* **2018**, *2*, 788−798.

(15) Tsikritzis, D.; Rogdakis, K.; Chatzimanolis, K.; Petrović, M.; Tzoganakis, N.; Najafi, L.; Martín-García, B.; Oropesa-Nuñez, R.; Bellani, S.; Del Rio Castillo, A. E.; Prato, M.; Stylianakis, M. M.; Bonaccorso, F.; Kymakis, E. A Two-Fold Engineering Approach Based on Bi₂Te₃ Flakes Towards Efficient and Stable Inverted Perovskite Solar Cells. *Mater. Adv.* **2020**, *1*, 450−462.

(16) Park, S.; Heo, J. H.; Yun, J. H.; Jung, T. S.; Kwak, K.; Ko, M. J.; Cheon, C. H.; Kim, J. Y.; Im, S. H.; Son, H. J. Effect of Multi-Armed

Triphenylamine-Based Hole Transporting Materials for High Performance Perovskite Solar Cells. *Chem. Sci.* **2016**, *7*, 5517−5522.

(17) Agresti, A.; Pescetelli, S.; Palma, A. L.; Martín-García, B.; Najafi, L.; Bellani, S.; Moreels, I.; Prato, M.; Bonaccorso, F.; Di Carlo, A. Two-Dimensional Material Interface Engineering for Efficient Perovskite Large-Area Modules. *ACS Energy Lett.* **2019**, *4*, 1862−1871.

(18) Taheri, B.; Yaghoobi Nia, N.; Agresti, A.; Pescetelli, S.; Ciceroni, C.; Del Rio Castillo, A. E.; Cinà, L.; Bellani, S.; Bonaccorso, F.; Di Carlo, A. Graphene-Engineered Automated Sprayed Mesoscopic Structure for Perovskite Device Scaling-up. *2D Mater.* **2018**, *5*, 045034.

(19) Qin, P.; Tetreault, N.; Dar, M. I.; Gao, P.; McCall, K. L.; Rutter, S. R.; Ogier, S. D.; Forrest, N. D.; Bissett, J. S.; Simms, M. J.; et al. A Novel Oligomer as a Hole Transporting Material for Efficient Perovskite Solar Cells. *Adv. Energy Mater.* **2015**, *5*, 1400980.

(20) Park, N.-G.; Miyasaka, T.; Grätzel, M. *Organic-Inorganic Halide Perovskite Photovoltaics*; Springer: Cham, Switzerland, 2016.

(21) Azadinia, M.; Ameri, M.; Ghahrizjani, R. T.; Fathollahi, M. Maximizing the Performance of Single and Multijunction MA and Lead-Free Perovskite Solar Cell. *Mater. Today Energy* **2021**, *20*, 100647.

(22) Wang, B.; Yang, J.; Lu, L.; Xiao, W.; Wu, H.; Xiong, S.; Tang, J.; Duan, C.; Bao, Q. Interface Engineering of Air-Stable n-Doping Fullerene-Modified TiO₂ Electron Transport Layer for Highly Efficient and Stable Perovskite Solar Cells. *Adv. Mater. Interfaces* **2020**, *7*, 1901964.

(23) Mohamad Noh, M. F.; Teh, C. H.; Daik, R.; Lim, E. L.; Yap, C. C.; Ibrahim, M. A.; Ahmad Ludin, N.; Mohd Yusoff, A. R. b.; Jang, J.; Mat Teridi, M. A.; Teridi, M. A. M. The Architecture of the Electron Transport Layer for a Perovskite Solar Cell. *J. Mater. Chem. C* **2018**, *6*, 682.

(24) Zanetta, A.; Bulfaro, I.; Faini, F.; Manzi, M.; Pica, G.; De Bastiani, M.; Bellani, S.; Zappia, M. I.; Bianca, G.; Gabatel, L.; Panda, J. K.; Del Rio Castillo, A. E.; Prato, M.; Lauciello, S.; Bonaccorso, F.; Grancini, G. Enhancing Charge Extraction in Inverted Perovskite Solar Cells Contacts via Ultrathin Graphene: Fullerene Composite Interlayers. *J. Mater. Chem. A* **2023**, *11*, 12866−12875.

(25) Najafi, L.; Bellani, S.; Gabatel, L.; Zappia, M. I.; Di Carlo, A.; Bonaccorso, F. Reverse-Bias and Temperature Behaviors of Perovskite Solar Cells at Extended Voltage Range. *ACS Appl. Energy Mater.* **2022**, *5*, 1378−1384.

(26) Agarwala, P.; Kabra, D. A Review on Triphenylamine (TPA) Based Organic Hole Transport Materials (HTMs) for Dye Sensitized Solar Cells (DSSCs) and Perovskite Solar Cells (PSCs): Evolution and Molecular Engineering. *J. Mater. Chem. A* **2017**, *5*, 1348−1373.

(27) Huckaba, A. J.; Sanghyun, P.; Grancini, G.; Bastola, E.; Taek, C. K.; Younghui, L.; Bhandari, K. P.; Ballif, C.; Ellingson, R. J.; Nazeeruddin, M. K. Exceedingly Cheap Perovskite Solar Cells Using Iron Pyrite Hole Transport Materials. *ChemistrySelect* **2016**, *1*, 5316−5319.

(28) Pashaei, B.; Shahroosvand, H.; Ameri, M.; Mohajerani, E.; Nazeeruddin, M. K. A Sequential Condensation Route as a Versatile Platform for Low Cost and Efficient Hole Transport Materials in Perovskite Solar Cells. *J. Mater. Chem. A* **2019**, *7*, 21867−21873.

(29) Magomedov, A.; Paek, S.; Gratia, P.; Kasparavicius, E.; Daskeviciene, M.; Kamarauskas, E.; Gruodis, A.; Jankauskas, V.; Kantminiene, K.; Cho, K. T.; et al. Diphenylamine-Substituted Carbazole-Based Hole Transporting Materials for Perovskite Solar Cells: Influence of Isomeric Derivatives. *Adv. Funct. Mater.* **2018**, *28*, 1704351.

(30) Matebese, F.; Taziwa, R.; Mutukwa, D. Progress on the Synthesis and Application of CuSCN Inorganic Hole Transport Material in Perovskite Solar Cells. *Materials* **2018**, *11*, 2592.

(31) Marsitzky, D.; Murray, J.; Scott, J. C.; Carter, K. R. Amorphous Poly-2, 7-Fluorene Networks. *Chem. Mater.* **2001**, *13*, 4285−4289.

(32) Jeong, M.; Choi, I. W.; Go, E. M.; Cho, Y.; Kim, M.; Lee, B.; Jeong, S.; Jo, Y.; Choi, H. W.; Lee, J.; et al. Stable Perovskite Solar

Cells with Efficiency Exceeding 24.8% and 0.3-V Voltage Loss. *Science* **2020**, *369*, 1615−1620.

(33) Malinauskas, T.; Tomkute-Luksiene, D.; Sens, R. D.; Daskeviciene, M.; Send, R.; Wonneberger, H.; Jankauskas, V.; Bruder, I.; Getautis, V. Enhancing Thermal Stability and Lifetime of Solid-State Dye-Sensitized Solar Cells via Molecular Engineering of the Hole-Transporting Material Spiro-OMeTAD. *ACS Appl. Mater. Interfaces* **2015**, *7*, 11107−11116.

(34) Zhao, X.; Kim, H.-S.; Seo, J.-Y.; Park, N.-G. Effect of Selective Contacts on the Thermal Stability of Perovskite Solar Cells. *ACS Appl. Mater. Interfaces* **2017**, *9*, 7148−7153.

(35) Wang, Y. K.; Yuan, Z. C.; Shi, G. Z.; Li, Y. X.; Li, Q.; Hui, F.; Sun, B. Q.; Jiang, Z. Q.; Liao, L. S. Dopant-Free Spiro-Triphenyl-amine/Fluorene as Hole-Transporting Material for Perovskite Solar Cells with Enhanced Efficiency and Stability. *Adv. Funct. Mater.* **2016**, *26*, 1375−1381.

(36) Pastore, M.; Etienne, T.; De Angelis, F. Structural and Electronic Properties of Dye-Sensitized TiO$_2$ for Solar Cell Applications: From Single Molecules to Self-Assembled Monolayers. *J. Mater. Chem. C* **2016**, *4*, 4346−4373.

(37) Osedach, T. P.; Andrew, T. L.; Bulović, V. Effect of Synthetic Accessibility on the Commercial Viability of Organic Photovoltaics. *Energy Environ. Sci.* **2013**, *6*, 711.

(38) Murray, A. T.; Frost, J. M.; Hendon, C. H.; Molloy, C. D.; Carbery, D. R.; Walsh, A. Modular Design of SPIRO-OMeTAD Analogues as Hole Transport Materials in Solar Cells. *Chem. Commun.* **2015**, *51*, 8935−8938.

(39) Zhang, J.; Zhang, T.; Jiang, L.; Bach, U.; Cheng, Y.-B. 4-tert-Butylpyridine Free Hole Transport Materials for Efficient Perovskite Solar Cells: A New Strategy to Enhance the Environmental and Thermal Stability. *ACS Energy Lett.* **2018**, *3*, 1677−1682.

(40) Habisreutinger, S. N.; Wenger, B.; Snaith, H. J.; Nicholas, R. J. Dopant-Free Planar n−i−p Perovskite Solar Cells with Steady-State Efficiencies Exceeding 18%. *ACS Energy Lett.* **2017**, *2*, 622−628.

(41) Wang, S.; Yuan, W.; Meng, Y. S. Spectrum-Dependent Spiro-OMeTAD Oxidization Mechanism in Perovskite Solar Cells. *ACS Appl. Mater. Interfaces* **2015**, *7*, 24791−24798.

(42) Jiang, K.; Wu, F.; Zhang, G.; Zhu, L.; Yan, H. Efficient perovskite solar cells based on dopant-free spiro-OMeTAD processed with halogen-free green solvent. *Sol. RRL* **2019**, *3*, 1900061.

(43) Lu, H.; He, B.; Ji, Y.; Shan, Y.; Zhong, C.; Xu, J.; LiuYang, J.; Wu, F.; Zhu, L. Dopant-free hole transport materials processed with green solvent for efficient perovskite solar cells. *Chem. Eng. J.* **2020**, *385*, 123976.

(44) Yu, W.; Zhang, J.; Wang, X.; Liu, X.; Tu, D.; Zhang, J.; Guo, X.; Li, C. A Dispiro-Type Fluorene-Indenofluorene-Centered Hole Transporting Material for Efficient Planar Perovskite Solar Cells. *Sol. RRL* **2018**, *2*, 1800048.

(45) Connell, A.; Wang, Z.; Lin, Y.-H.; Greenwood, P. C.; Wiles, A. A.; Jones, E. W.; Furnell, L.; Anthony, R.; Kershaw, C. P.; Cooke, G.; et al. Low Cost Triazatruxene Hole Transporting Material for> 20% Efficiency Perovskite Solar Cells. *J. Mater. Chem. C* **2019**, *7*, 5235−5243.

(46) Abdellah, I. M.; Chowdhury, T. H.; Lee, J.-J.; Islam, A.; Nazeeruddin, M. K.; Gräetzel, M.; El-Shafei, A. Facile and Low-Cost Synthesis of a Novel Dopant-Free Hole Transporting Material That Rivals Spiro-OMeTAD for High Efficiency Perovskite Solar Cells. *Sustainable Energy Fuels* **2021**, *5*, 199−211.

(47) Jeon, N. J.; Lee, H. G.; Kim, Y. C.; Seo, J.; Noh, J. H.; Lee, J.; Seok, S. I. *o*-Methoxy Substituents in Spiro-OMeTAD for Efficient Inorganic−Organic Hybrid Perovskite Solar Cells. *J. Am. Chem. Soc.* **2014**, *136*, 7837−7840.

(48) Zhu, X. D.; Ma, X. J.; Wang, Y. K.; Li, Y.; Gao, C. H.; Wang, Z. K.; Jiang, Z. Q.; Liao, L. S. Hole-Transporting Materials Incorporating Carbazole into Spiro-Core for Highly Efficient Perovskite Solar Cells. *Adv. Funct. Mater.* **2019**, *29*, 1807094.

(49) Hu, Z.; Tang, G.; Miao, J.; Fu, T.; Li, T.; Tai, Q.; Meng, H.; Yan, F. π-Extended Spiro Core-Based Nonfullerene Electron-Trans-

(50) Eseola, A. O.; Adepitan, O.; Görls, H.; Plass, W. Electronic/Substituents Influence on Imidazole Ring Donor−Acceptor Capacities Using 1 H-imidazo [4, 5-f] [1, 10] Phenanthroline Frameworks. *New J. Chem.* **2012**, *36*, 891.

(51) Hajikhanmirzaei, L.; Shahroosvand, H.; Pashaei, B.; Monache, G. D.; Nazeeruddin, M. K.; Pilkington, M. K. M. A Cost-Device Efficiency Balanced Spiro Based Hole Transport Material for Perovskite Solar Cells. *J. Mater. Chem. C* **2020**, *8*, 6221−6227.

(52) Cardona, C. M.; Li, W.; Kaifer, A. E.; Stockdale, D.; Bazan, G. C. Electrochemical Considerations for Determining Absolute Frontier Orbital Energy Levels of Conjugated Polymers for Solar Cell Applications. *Adv. Mater.* **2011**, *23*, 2367−2371.

(53) Kong, F.; Gao, Y.; Ling, J.; Liu, Q. 2-(4-Methoxyphenyl) Phenanthro [9, 10-d] Imidazole Methanol Solvate. *Acta Crystallogr. E* **2008**, *64*, o156.

(54) Zheng, X.; Ma, Z.; Zhang, D. Synthesis of Imidazole-Based Medicinal Molecules Utilizing the Van Leusen Imidazole Synthesis. *Pharmaceuticals* **2020**, *13*, 37.

(55) Idris, M.; Coburn, C.; Fleetham, T.; Milam-Guerrero, J.; Djurovich, P. I.; Forrest, S. R.; Thompson, M. E. Phenanthro [9, 10-d] Triazole and Imidazole Derivatives: High Triplet Energy Host Materials for Blue Phosphorescent Organic Light Emitting Devices. *Mater. Horiz.* **2019**, *6*, 1179−1186.

(56) Sworakowski, J.; Lipiński, J.; Janus, K. On the Reliability of Determination of Energies of HOMO and LUMO Levels in Organic Semiconductors from Electrochemical Measurements. A Simple Picture Based on the Electrostatic Model. *Org. Electron.* **2016**, *33*, 300.

(57) Leonat, L.; Sbarcea, G.; Branzoi, I. V. Cyclic Voltammetry for Energy Levels Estimation of Organic Materials. *UPB Sci. Bull. B: Chem. Mater. Sci.* **2013**, *75*, 111−118.

(58) Hailegnaw, B.; Kirmayer, S.; Edri, E.; Hodes, G.; Cahen, D. Rain on Methylammonium Lead Iodide Based Perovskites: Possible Environmental Effects of Perovskite Solar Cells. *J. Phys. Chem. Lett.* **2015**, *6*, 1543−1547.

(59) Leijtens, T.; Ding, I.-K.; Giovenzana, T.; Bloking, J. T.; McGehee, M. D.; Sellinger, A. Hole Transport Materials with Low Glass Transition Temperatures and High Solubility for Application in Solid-State Dye-Sensitized Solar Cells. *ACS Nano* **2012**, *6*, 1455−1462.

(60) Odabaşı, Ç.; Yıldırım, R. Performance Analysis of Perovskite Solar Cells in 2013−2018 Using Machine-Learning Tools. *Nano Energy* **2019**, *56*, 770.

(61) Kaixiang, S. Research Progress and Design Strategy of Hole Transport Materials for Perovskite Solar Cells. *IOP Conf. Ser.: Earth Environ. Sci.* **2019**, *332*, 032030.

(62) Tsikritzis, D.; Chatzimanolis, K.; Tzoganakis, N.; Bellani, S.; Zappia, M. I.; Bianca, G.; Curreli, N.; Buha, J.; Kriegel, I.; Antonatos, N.; Sofer, Z.; Krassas, M.; Rogdakis, K.; Bonaccorso, F.; Kymakis, E. Two-Dimensional BiTeI as a Novel Perovskite Additive for Printable Perovskite Solar Cells. *Sustainable Energy Fuels* **2022**, *6*, 5345−5359.

(63) Calio, L.; Kazim, S.; Grätzel, M.; Ahmad, S. Hole-Transport Materials for Perovskite Solar Cells. *Angew. Chem., Int. Ed.* **2016**, *55*, 14522−14545.

(64) Burschka, J.; Pellet, N.; Moon, S.-J.; Humphry-Baker, R.; Gao, P.; Nazeeruddin, M. K.; Grätzel, M. Sequential Deposition as a Route to High-Performance Perovskite-Sensitized Solar Cells. *Nature* **2013**, *499*, 316−319.

(65) Zhang, Y.; Zhang, L.; Wang, R.; Pan, X. Theoretical Study on the Electronic Structure and Optical Properties of Carbazole-π-dimesitylborane as Bipolar Fluorophores for Nondoped Blue OLEDs. *J. Mol. Graphics Modell.* **2012**, *34*, 46−56.

(66) Zhao, C.; Wang, W.; Ma, Y. Molecular Design Toward Good Hole Transport Materials Based on Anthra [2, 3-c] Thiophene: A Theoretical Investigation. *Comput. Theor. Chem.* **2013**, *1010*, 25−31.

(67) Salehi Taleghani, S.; Zamani Meymian, M. R.; Ameri, M. Interfacial Modification to Optimize Stainless Steel Photoanode Design for Flexible Dye Sensitized Solar Cells: an Experimental and

Numerical Modeling Approach. *J. Phys. D: Appl. Phys.* **2016**, *49*, 405601.

(68) Najafi, L.; Taheri, B.; Martin-Garcia, B.; Bellani, S.; Di Girolamo, D.; Agresti, A.; Oropesa-Nunez, R.; Pescetelli, S.; Vesce, L.; Calabro, E.; Prato, M.; Del Rio Castillo, A. E.; Di Carlo, A.; Bonaccorso, F. MoS_2 Quantum Dot/Graphene Hybrids for Advanced Interface Engineering of a $CH_3NH_3PbI_3$ Perovskite Solar Cell with an Efficiency of over 20. *ACS Nano* **2018**, *12*, 10736−10754.

(69) Kang, M. S.; Sung, S. D.; Choi, I. T.; Kim, H.; Hong, M.; Kim, J.; Lee, W. I.; Kim, H. K. Novel Carbazole-Based Hole-Transporting Materials with Star-Shaped Chemical Structures for Perovskite-Sensitized Solar Cells. *ACS Appl. Mater. Interfaces* **2015**, *7*, 22213−22217.

(70) Wazzan, N.; Safi, Z. Effect of Number and Position of Methoxy Substituents on Fine-Tuning the Electronic Structures and Photo-physical Properties of Designed Carbazole-Based Hole-Transporting Materials for Perovskite Solar Cells: DFT Calculations. *Arab. J. Chem.* **2019**, *12*, 1.